








**Tin resonance-ionization schemes for atomic- and nuclear-structure studies**

F. P. Gustafsson <sup>1</sup>, C. M. Ricketts <sup>2</sup>, M. L. Reitsma <sup>3</sup>, R. F. Garcia Ruiz,<sup>4,5</sup> S. W. Bai,<sup>6</sup> J. C. Berengut <sup>7,8</sup>, J. Billowes,<sup>2</sup> C. L. Binnersley,<sup>2</sup> A. Borschevsky <sup>3</sup>, T. E. Cocolios,<sup>1</sup> B. S. Cooper,<sup>2</sup> R. P. de Groote,<sup>9</sup> K. T. Flanagan,<sup>2,10</sup> Á. Koszorús,<sup>1,\*</sup> G. Neyens <sup>1,5</sup>, H. A. Perrett,<sup>2</sup> A. R. Vernon,<sup>1,2</sup> Q. Wang,<sup>5,†</sup> S. G. Wilkins,<sup>11</sup> and X. F. Yang <sup>6</sup>

<sup>1</sup>*KU Leuven, Instituut voor Kern- en Stralingsfysica, B-3001 Leuven, Belgium*

<sup>2</sup>*School of Physics and Astronomy, The University of Manchester, Manchester M13 9PL, United Kingdom*

<sup>3</sup>*Van Swinderen Institute for Particle Physics and Gravity, University of Groningen, Nijenborgh 4, 9747AG Groningen, The Netherlands*

<sup>4</sup>*Massachusetts Institute of Technology, Cambridge, Massachusetts 02139, USA*

<sup>5</sup>*EP Department, CERN, CH-1211 Geneva 23, Switzerland*

<sup>6</sup>*School of Physics and State Key Laboratory of Nuclear Physics and Technology, Peking University, Beijing 100871, China*

<sup>7</sup>*Max-Planck-Institut für Kernphysik, Saupfercheckweg 1, 69117 Heidelberg, Germany*

<sup>8</sup>*School of Physics, University of New South Wales, New South Wales 2052, Australia*

<sup>9</sup>*Department of Physics, University of Jyväskylä, PB 35 (YFL) FIN-40351 Jyväskylä, Finland*

<sup>10</sup>*Photon Science Institute, Alan Turing Building, The University of Manchester, Manchester M13 9PY, United Kingdom*

<sup>11</sup>*EN Department, CERN, CH-1211 Geneva 23, Switzerland*



(Received 7 September 2020; accepted 20 October 2020; published 13 November 2020)

This paper presents high-precision spectroscopic measurements of atomic tin using five different resonance-ionization schemes performed with the collinear resonance-ionization spectroscopy technique. Isotope shifts were measured for the stable tin isotopes from the  $5s^25p^2\ ^3P_{0,1,2}$  and  $^1S_0$  to the  $5s^25p6s\ ^1P_1$ ,  $^3P_{1,2}$  and  $5s^25p7s\ ^1P_1$  atomic levels. The magnetic dipole hyperfine constants  $A_{\text{hf}}$  have been extracted for six atomic levels with electron angular momentum  $J > 0$  from the hyperfine structures of nuclear spin  $I = 1/2$  tin isotopes,<sup>115,117,119</sup>Sn. State-of-the-art atomic calculations using a relativistic Fock-space coupled-cluster method and the configuration interaction approach combined with many-body perturbation theory allow accurate and reliable calculations of both field- and mass-shift factors for the studied transitions, in addition to the hyperfine magnetic fields and electric-field gradients of the atomic levels. The excellent agreement with the experimental results highlights the accuracy of modern atomic theory and establishes an important foundation for precision measurements of nuclear moments and charge radii of the most exotic isotopes of tin.

DOI: [10.1103/PhysRevA.102.052812](https://doi.org/10.1103/PhysRevA.102.052812)

**I. INTRODUCTION**

Atomic and ionic spectral lines are observed to shift between different isotopes of the same element. The isotope shift can be extracted using various optical methods, even for short-lived radioactive isotopes [1]. Precision measurements of isotope shifts, which are usually smaller than 1 part in  $10^6$  of the absolute transition frequency, provide insight into the electron-nucleus interaction and allow systematic studies of changes in nuclear charge radii [2,3] or probing of fundamental interactions [4–6]. This requires an accurate understanding of the atomic field- and mass-shift factors for decoupling the atomic-physics contribution [7,8]. Furthermore, the electronic fine-structure levels split into sublevels known as the

hyperfine structure (HFS) for atoms containing nuclei with nonzero spin. This splitting can be attributed to the presence of nonzero nuclear electromagnetic moments and depends on the hyperfine magnetic field and, for spin greater than  $1/2$ , on the electric-field gradient (EFG) generated by the electrons.

Until recently, field and mass shifts, hyperfine magnetic fields, and EFGs remained difficult to calculate with high accuracy for multielectron systems [7,9,10]. To calculate these properties, a sophisticated treatment of electron correlations and relativistic effects is required. Measurements of HFS constants of multielectron systems can, therefore, be of great value for validating modern electronic structure methods [11–14]. Furthermore, nuclear moments and charge radii, regularly extracted from the HFS and isotope shift measurements of stable and radioactive isotopes, are valuable for studies of nuclear structure [1–3,15–17]. Longstanding questions on the evolution of these nuclear structure observables towards the limits of existence test our description of the nuclear many-body problem.

Tin, having a closed shell for protons within the nuclear shell model ( $Z = 50$ ), has the largest number of stable isotopes of all known elements, featuring seven even-mass spin-0 isotopes<sup>112,114,116,118,120,122,124</sup>Sn, and three spin- $1/2$  isotopes<sup>115,117,119</sup>Sn. For this reason, the tin isotopic chain provides

\*Present address: Oliver Lodge Laboratory, Oxford Street, University of Liverpool, Liverpool L69 7ZE, United Kingdom.

†On leave from: Lanzhou University, 222 Tianshui S Road, Chengguan, Lanzhou, Gansu, China.

Published by the American Physical Society under the terms of the [Creative Commons Attribution 4.0 International license](https://creativecommons.org/licenses/by/4.0/). Further distribution of this work must maintain attribution to the author(s) and the published article's title, journal citation, and DOI.

an excellent case for investigating the influence of nuclear charge radii and nuclear magnetic dipole moments on the hyperfine structure of different atomic states. Moreover, tin is of particular interest for nuclear structure studies, as it is the heaviest known element containing two isotopes with both closed neutron and proton shells: the neutron-deficient  $^{100}\text{Sn}$  and the neutron-rich  $^{132}\text{Sn}$  [18–21]. Significant efforts have been made to perform laser spectroscopy across the tin chain reaching from  $^{134}\text{Sn}$  down to  $^{108}\text{Sn}$  [20,22–25]. Further laser-spectroscopy measurements are planned, both at existing facilities and in new laboratories currently under construction [26–28]. All proposed experimental methods aim to achieve high signal-detection efficiency and low background, a requirement to allow the study of exotic isotopes with low production rates when approaching  $^{100}\text{Sn}$ . For example, at the ISOLDE radioactive beam facility of CERN,  $^{101}\text{Sn}$  with a half-life of only 1.9(3) s [29] is predicted to be produced at a rate of less than one ion per second. A campaign for studying the neutron-deficient tin isotopes is ongoing at the Collinear Resonance Ionization Spectroscopy (CRIS) experiment at ISOLDE [26]. Other high-precision and sensitive laser-ionization-spectroscopy techniques are being developed, such as the perpendicularly illuminated laser ion source and trap (PI-LIST) method [30] and the in-gas-jet laser-spectroscopy method [31]. All these methods share a common need for well-understood laser-ionization schemes. These schemes have to be optimized specifically for the element of interest, with optimal sensitivity to the nuclear observables.

In this work, several laser-ionization schemes are evaluated, through measurements of isotope shifts and hyperfine-structure constants of all stable tin isotopes. Since there are no stable tin isotopes with nuclear spin greater than  $I = 1/2$ , there is no measurable electric quadrupole interaction between the nucleus and the surrounding electrons. Calculations of the EFGs are therefore required to evaluate the sensitivity of the atomic states to the spectroscopic nuclear electric quadrupole moment. The state-of-the-art relativistic Fock-space coupled-cluster (FSCC) approach was used for calculating the EFGs, hyperfine magnetic fields, and field-shift factors, while the configuration interaction approach with many-body perturbation theory (CI+MBPT) was used to calculate the mass-shift factors. The calculated atomic factors are validated by the experimental data and other measurements from the recent literature.

This paper is organized as follows. The CRIS technique used to perform the measurements is described in Sec. II, from the production of the ions of naturally abundant tin, to the collinear resonance ionization and ion detection. A detailed description of the laser setup used to generate the light required for laser ionization is further described, followed by a description of the data collection procedure. In Sec. III, the theoretical methods used in this work are introduced and the procedures used for calculating the field- and mass-shift factors, hyperfine magnetic fields, and EFGs are presented. Section IV introduces the data handling and analysis strategy that was followed to extract the atomic observables and their corresponding uncertainties. The hyperfine  $A_{\text{hf}}$  constants for all investigated atomic states in the odd-mass isotopes  $^{115,117,119}\text{Sn}$  are presented and compared with the literature,

as are the isotope shifts for all transitions employed in this work. These results are discussed in Sec. V. In Sec. VA, the calculated field- and mass-shift factors are compared with experimental values deduced from a King-plot analysis against mean-square nuclear charge radii evaluated from a combined analysis of atomic spectroscopy, muonic x-ray, and electron-scattering data. Then, using the calculated field- and mass-shift factors, independent sets of root-mean-square (rms) nuclear charge radii for all stable isotopes of tin are deduced for two of the studied transitions and compared with the literature. Both approaches show that reliable field- and mass-shift factors are calculated. In Sec. VB, the hyperfine magnetic fields extracted from the data are compared with the theoretical predictions and experimental data from other work. This is followed by Sec. VC, where the calculated EFGs of the studied atomic levels are provided. The paper is concluded with a summary in Sec. VD.

## II. EXPERIMENTAL SETUP

### A. Ion source and the CRIS beam line

The ion source and the CRIS beam line [2,32,33] at ISOLDE-CERN are shown schematically in Fig. 1. A bunched ion beam containing all stable isotopes of tin was generated by laser ablation of a solid tin target (>99% purity). A 532 nm Nd:YAG laser was used for the ablation, operating at 100 Hz repetition rate and with approximately 30 mJ/pulse, focused onto the tin target, with a spot diameter less than 1 mm. The interaction with the laser pulse generated a plume of tin ions which was extracted by a low electric field. A detailed description of this unit is presented in Ref. [34]. The bunched beam of tin ions was accelerated with a voltage selected between 20 and 30 kV. By electrostatically steering the beam through a heated charge-exchange cell (CEC), which contains sodium vapor at 230–250 °C, the beam was partially neutralized. The fraction of neutral tin atoms within the beam varied between 10 and 30%, depending on the vapor pressure of the sodium. Different atomic states in Sn I were populated [35]. The partially neutralized beam leaving the CEC passed an electric-field gradient of 5000 V/cm perpendicular to its path, thereby removing ions and field-ionizing atoms neutralized into high-lying Rydberg states, before entering a differential pumping region held at a pressure of  $5 \times 10^{-9}$  mbar. Residual ions collisionally ionized in the differential pumping region were removed from the beam after passing an electric field of 1000 V/cm before entering the interaction region, which is kept at an ultrahigh vacuum of  $5 \times 10^{-10}$  mbar. Within the interaction region, each atom bunch was collinearly overlapped in space and synchronized in time with a series of laser pulses: first, a tunable high-resolution pulse which, when in resonance with the chosen atomic transition, excited the atomic electrons to a higher-lying atomic state. For the three-step ionization schemes, a second laser pulse resonantly excited the atoms into an even higher-lying state, before a third high-power laser pulse nonresonantly ionized the excited atoms. Performing this resonance-ionization process in flight reduces the Doppler broadening by a factor of  $10^3$ , often reaching the magnitude of the intrinsic width of the atomic transition [36]. Ions present in the bunch were then electrostatically deflected and counted

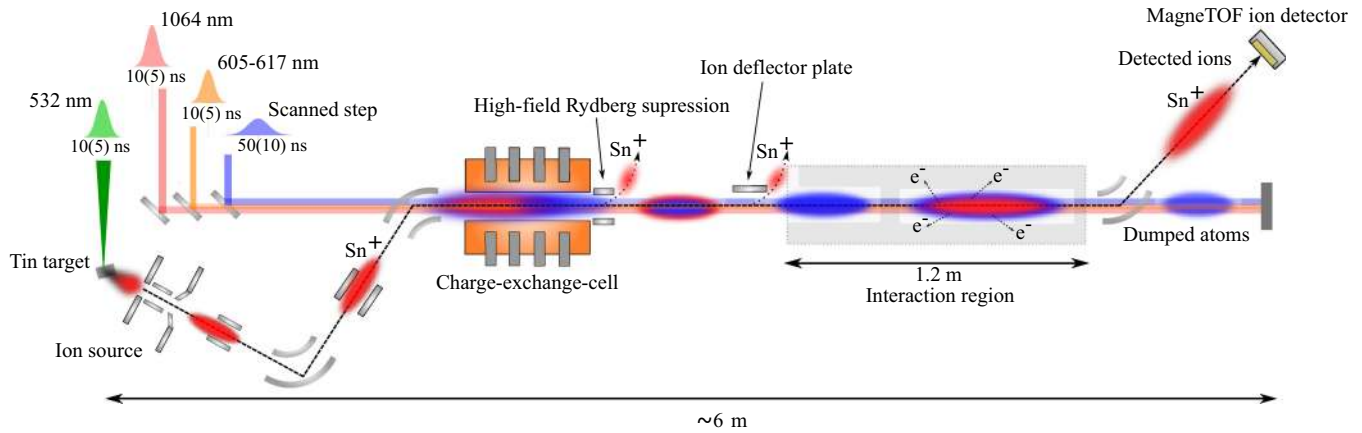


FIG. 1. Schematic overview of the CRIS beam line and the laser ablation ion source. The ions, indicated in red, are extracted from the solid tin target, accelerated, and steered through a charge-exchange cell. Here, the ions neutralize; only the atoms, indicated in blue, pass the high-field Rydberg suppression plates and the ion deflector before entering the interaction region. In the interaction region, laser pulses are collinearly overlapped with the atomic bunch in both time and space, resulting in stepwise excitation and ionization of the atoms when on resonance. The ions are separated from the remaining background atoms and detected with an ETP MagneTOF ion detector.

using an ETP DM291 MagneTOF detector. Any remaining atoms do not reach the detector, resulting in a low detected background signal.

### B. Lasers

The tested laser-ionization schemes are shown in Fig. 2. The first laser step for all indicated ionization schemes was scanned in frequency in order to measure the hyperfine structures and isotope shifts. The narrowband laser pulses, required to resolve these effects, were generated from an injection-locked Ti:sapphire laser system [37] seeded with continuous-wave light produced by either an M-Squared SolisTiS or a Sirah Matisse Ti:sapphire laser system. This seeded laser is pumped using a Q-switched Nd:YAG laser (Lee Laser LDP-100MQG) at 1 kHz. In order to reach 266–286 nm, a

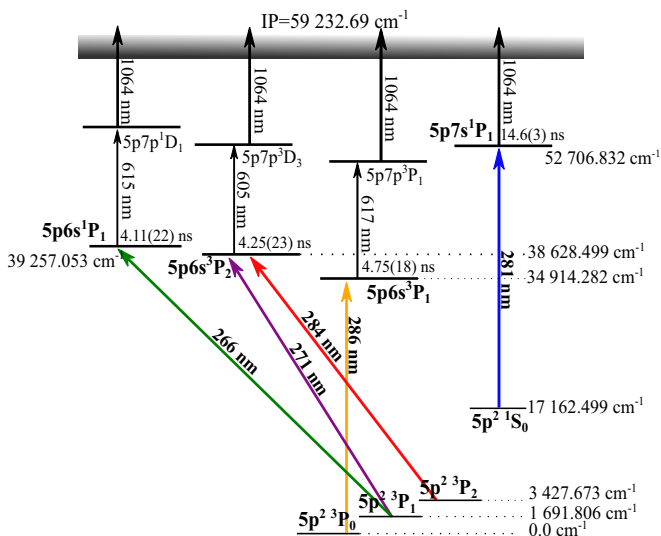


FIG. 2. Tin ionization schemes studied in this work. Lifetimes are taken from Ref. [39] and level energies from Ref. [41].

sum-harmonic generation unit, using two nonlinear crystals, i.e., bismuth borate (BIBO) and beta barium borate (BBO) crystals, was used. This provided laser pulses with a linewidth of the order of 60 MHz, a pulse length of 50(10) ns, and energy of 30–150 nJ/pulse. The laser frequency of the seed light was scanned at a rate below 5 MHz/s over the frequency region containing all stable tin isotopes and was continuously measured using a WSU-2 HighFinesse wave meter. This wave meter also recorded a reference wavelength from a stabilized laser diode (Toptica DLC DL PRO 780) locked to the Doppler-free hyperfine transition  $5S_{1/2}(F=2) - 5P_{3/2}(F'=3)$  of  $^{87}\text{Rb}$  (TEM CoSy). This was used to correct for drifts in the wave-meter readout over the course of the experiment [38]. In most cases, a second resonant step was used with a wavelength of 605–617 nm, a pulse energy of 50–200  $\mu\text{J}$ /pulse, and a pulse length of 10(5) ns. This laser light was produced with a SPECTRON SL4000 pulsed dye laser system, using DCM dye dissolved in ethanol. This dye laser was pumped using one of the 532 nm outputs from a dual-head Nd:YAG laser (Litron LPY 601 50-100 PIV), Q-switched at 100 Hz repetition rate. The second independent head provided pulsed laser light for laser ablation, thus defining the cycle length of measurements as 10 ms. The last nonresonant step is provided by a Nd:YAG laser (Litron TRLi 250-100) generating 50–100 mJ/pulse at 1064 nm with a pulse length of 10(5) ns and a repetition rate of 100 Hz. The delay and synchronization of all lasers was performed using a set of Quantum Composers 9528 digital-delay pulse generators. Due to the short half life of the first-excited states, which were all of the order of a few nanoseconds [39], all lasers were overlapped with a delay of 30(20) ns between subsequent pulses. Measurements of the full range of isotopes were repeated 2–3 times for each transition.

### C. Data-collection procedure

The resonantly ionized ions were registered on an event-by-event basis, with sub-ns timing resolution for time-of-flight

(TOF) determination from the pulsed laser-induced ablation production process to detection with an ETP MagneTOF detector, using a ChronoLogic TimeTagger4-2G time-to-digital card [40]. The frequency measurements of the first and second resonance steps including the reference diode were recorded every 10 ms in sync with the laser atom beam overlap. A time stamp for each measurement allowed the merging of frequency, TOF, and ion events which was binned with respect to frequency for generating a spectrum.

### III. ATOMIC THEORY

#### A. Field-shift and HFS parameter calculations

High-accuracy calculations of the properties of heavy atoms require a high-quality treatment of relativistic and electron correlation effects. Therefore, a state-of-the-art relativistic Fock-space coupled-cluster approach and a combination of the configuration interaction with the many-body perturbation theory were employed for the investigation of the HFS and isotope shift parameters. The multireference relativistic FSCC method [42,43], employed in this work for the calculation of the field shifts, EFGs, and the hyperfine magnetic field constants, is considered to be one of the most powerful approaches for heavy many-electron systems. Compared to single-reference methods, it has the distinct advantage of being able to treat many excited states with consistent quality. The calculations are carried out in the framework of the Dirac-Coulomb Hamiltonian,

$$H_0 = \sum_i h_D(i) + \frac{1}{2} \sum_{i \neq j} \frac{1}{r_{ij}}, \quad (1)$$

where  $h_D$  is the Dirac one-particle Hamiltonian,

$$h_D(i) = c \boldsymbol{\alpha}_i \cdot \mathbf{p}_i + c^2(\beta_i - 1) + V_{eN}(i), \quad (2)$$

and  $\alpha$  and  $\beta$  are the Dirac matrices. The Coulomb potential  $V_{eN}(i)$  is the electron-nucleus interaction, with the nuclear charge distribution modeled by a Gaussian function as described in Ref. [44].

The FSCC method requires a closed-shell reference state from which the ground state and the excited states can be reached by adding or removing electrons. In the case of neutral tin, which has an open-shell ground-state electron configuration  $[\text{Kr}]4d^{10}5s^25p^2$ , the closed-shell  $\text{Sn}^{2+}$  system ( $[\text{Kr}]4d^{10}5s^2$ ) is used as the reference state and two electrons are added to the orbitals that comprise the model space,  $P$ . By including the  $5p$  orbital in  $P$ , the  $5p^2$  configurations including the ground state of neutral tin are obtained. By allowing the electrons to occupy higher virtual orbitals, further excited states of interest can be included in the calculation. A larger model space also increases the accuracy because of the correlation contribution from the additional states. The use of large model spaces can, however, cause convergence difficulties due to the existence of close-lying states in the virtual space that couple strongly to the model-space states. The intermediate Hamiltonian (IH) approach [45] was applied to avoid this problem. In this method, the model space is divided into a main space  $P_m$  and an intermediate space  $P_i$  and the problematic amplitudes between the  $P_i$  and the virtual space are removed.

The field-shift factors  $F_\lambda$  are obtained by performing FSCC calculations of the transition energies for several values of  $\langle r^2 \rangle$  by modifying the exponent of the Gaussian function describing the nuclear charge distribution [44]. The derivative of the energy with respect to  $\langle r^2 \rangle$  then gives the field-shift factor for each transition.

The finite field method [46] was used for the calculation of the EFG ( $q$ ) and the magnetic field at the core,  $A_0$ , as described in Refs. [11,47]. The desired property is added to the Dirac-Coulomb Hamiltonian [Eq. (1)] as a perturbation  $H'$  with strength  $\lambda$ ,

$$H(\lambda) = H_0 + \lambda H'. \quad (3)$$

The total energy can then be expressed via the Taylor expansion,

$$E(\lambda) = E_0 + \lambda \left. \frac{dE_\lambda}{d\lambda} \right|_{\lambda=0} + \frac{\lambda^2}{2} \left. \frac{d^2E_\lambda}{d\lambda^2} \right|_{\lambda=0} + \dots \quad (4)$$

For small enough values of  $\lambda$ , higher-order terms can be ignored and the expectation value of  $H'$  can be obtained numerically, according to the Hellmann-Feynman theorem, from the first derivative of the energy with respect to  $\lambda$ ,

$$\left. \frac{dE(\lambda)}{d\lambda} \right|_{\lambda=0} = \langle \Psi | H' | \Psi \rangle. \quad (5)$$

The size of  $\lambda$  was chosen from two considerations: the perturbation must be large enough to avoid numerical errors, but small enough to stay in the linear regime where the higher-order terms can be neglected. The derivative is calculated from the two-point formula,

$$\left. \frac{dE_\lambda}{d\lambda} \right|_{\lambda=0} \approx \frac{E(\lambda) - E(-\lambda)}{2\lambda}. \quad (6)$$

In the case of the EFG calculation,  $H'$  is the interaction of the electric quadrupole moment  $Q$  with the EFG as given in Ref. [48]. Similarly for the calculation of  $A_0$ , the magnetic hyperfine interaction is added as a perturbation; further details can be found in Ref. [11]. By using the two-point formula, any quadratic terms cancel out, resulting in an error proportional to  $\lambda^2$ , as shown in Ref. [11]. Two versions of the DIRAC program package [49] were employed. The field-shift and EFG calculations were carried out using DIRAC15 [50], while DIRAC17 was used for the  $A_0$  calculations [51]. The calculations were performed using the exact two-component Hamiltonian (X2C) [52]. This approach allows a significant decrease in computational time and expense, while reproducing very well the results obtained using the full four-component dc Hamiltonian, as tested for a variety of species and properties [53,54]. A comparison of the X2C and full four-component results for a small basis set and model space yielded differences of the order of 0.5%, thus justifying the use of the former approximation. The Gaunt term was included at the Dirac-Hartree-Fock step of the calculations using a small basis set and model space for uncertainty estimation purposes. It is part of the Breit interaction that corrects the two-electron part of the Dirac-Coulomb Hamiltonian up to the order of  $(Z\alpha)^2$  [55].

An extensive investigation of the effect of various computational parameters (basis set, model space, etc.) on the



obtained results was carried out. The aim of this investigation was twofold. On the one hand, it allows one to identify the computational scheme where convergence of the obtained results is reached with respect to the various parameters, which is used to provide the final recommended values. On the other hand, this investigation is used to set uncertainties on our predictions.

The final recommended results are obtained using the relativistic core-valence 4-zeta basis set of Dyall [56] (cv4z), augmented by four diffuse functions in each symmetry in an even-tempered fashion. A large model space was used, consisting of the  $5p\ 6s\ (5d\ 6p\ 7s\ 4f\ 6d\ 7p\ 8s\ 5f\ 7d\ 5g\ 8p\ 9s\ 6f\ 8d\ 9p\ 6g\ 6h\ 7g\ 10p\ 10s\ 7f)$  orbitals, where the orbitals in parentheses are in the intermediate space  $P_i$ . All the electrons were correlated and virtual orbitals with energies up to 500 a.u. were included in the calculation. For the calculation of  $F_\lambda$ , a change in the radius  $\langle r^2 \rangle$  of approximately 20% was used, while the perturbation strength  $\lambda$  was  $5 \times 10^{-7}$  for the EFG calculations and  $10^{-4}$  for  $A_0$ . The remaining sources of error in these calculations are the basis-set incompleteness, neglect of higher-order relativistic effects (i.e., the full Breit and the QED corrections), and the residual correlation effects. The basis-set associated uncertainty is comprised of three parts to account for the basis-set quality, correlating functions, and augmentation. Basis-set quality was evaluated by comparing the results using a 3-zeta and the 4-zeta quality basis set. The effect of correlating functions is included by comparing the core-valence and all-electron basis-set results, while augmentation effects are included by comparing the results using a basis set augmented with three and with four diffuse functions in each symmetry. This adds up to 2% for all the values, except for the EFG and  $A_0$  of the  $5p7s\ ^1P_1$  and  $5p6s\ ^1P_1$  states with uncertainties of about 15% and about 8%, respectively, and 15% for the field-shift factor of the  $5p^2\ ^1S_0$  to  $5p7s\ ^1P_1$  transition. It is assumed that the error due to the incomplete treatment of the relativistic effects is not larger than the difference between the X2C and the four-component results, together with the Gaunt contribution. It is about 1% for all states and transitions considered here. The missing correlation effects are due to the limited size of the correlation space and the finite size of the model space. The error caused by the limited correlation space is estimated by comparison of calculations with a virtual space cutoff at 500 and 2000 a.u., which gives an uncertainty of less than 0.1% for each property. The finite size of the model space is taken into account by comparing calculations that use a model space that differs by one orbital in each symmetry, resulting in an uncertainty of 1% for all the states except the highest one, where the effect is larger and of the order of 10%. In the present calculations, excitations beyond doubles are neglected. As triple and higher excitations cannot presently be evaluated for these properties within the FSCC framework, a rigorous scheme for estimating their size is not available. However, these corrections are usually quite small and are not expected to exceed about 3%, based on similar HFS calculations in Ref. [11]. Combining the above sources of error and assuming them to be independent, the total conservative uncertainty estimate on the calculated values is 4% for all the states and transitions except for the EFG and

$A_0$  of the  $5p7s\ ^1P_1$  state, for which it is 18%, and the  $5p6s\ ^1P_1$  state that has an uncertainty of 9%, and 15% for the field-shift factor of the  $5p^2\ ^1S_0$  to  $5p7s\ ^1P_1$  transition. The presented uncertainties are dominated by the basis-set and correlation effects.

## B. Mass-shift calculations

To calculate the mass-shift factors, the combination of configuration interaction and many-body perturbation theory was used [57], implemented in the atomic structure code AMBIT (see [58] and references therein for full method and implementation details). These calculations start with Dirac-Fock equations to generate core orbitals and the  $V^{N-2}$  Dirac-Fock potential (which includes the electrostatic potential of core electrons from the closed-shell  $\text{Sn}^{2+}$  system). Valence and virtual orbitals were generated by diagonalizing a set of  $B$  splines over the Dirac-Fock operator [59].

A CI calculation was then performed including all single and double excitations from the reference configurations ( $5p^2$ ,  $5p\ 6s$ ,  $5p\ 7s$ ,  $5p\ 5d$ ) up to  $16spdf$ , which is close to saturation. In the CI+MBPT method, the two-electron Slater integrals are modified to include core-valence correlations to second order in the residual Coulomb interaction (formulas may be found in [60]). The MBPT basis includes all virtual orbitals up to  $30spdfg$ .

Despite making only a small contribution to the energy, configurations formed from excitations of the  $5s^2$  “core” shell are found to have a large impact on the specific mass shift. Therefore, the  $5s^2$  shell was removed from the MBPT expansion and included as a hole shell in the particle-hole CI+MBPT formalism [61]. Three-body MBPT diagrams [62] were included for any matrix elements involving the reference configurations listed above or the important  $5s\ 5p^3$  configuration.

To calculate the relativistic mass shift, the finite field approximation was used with the relativistic formulation [63–65]

$$H'_{\text{MS}} = \frac{1}{2M} \sum_{i,j} \left\{ \mathbf{p}_i \cdot \mathbf{p}_j - \frac{Z\alpha}{r_i} \left[ \boldsymbol{\alpha}_i + \frac{(\boldsymbol{\alpha}_i \cdot \mathbf{r}_i) \mathbf{r}_i}{r_i^2} \right] \cdot \mathbf{p}_j \right\}. \quad (7)$$

The mass shift can be separated into one-body and two-body operators, known as normal mass shift (NMS) and specific mass shift (SMS), respectively. In the Hamiltonian above, the normal mass shift is represented by terms with  $i = j$  and the specific mass shift is given by terms  $i \neq j$ . The coefficient  $k_{\text{MS}}$  is defined from the expectation value of  $H'_{\text{MS}}$  using the finite field method [Eq. (5)].

To estimate the uncertainties, the calculation is repeated using a four-valence-electron approximation. While this is identical at the CI level to using the particle-hole formalism, the MBPT diagrams are changed considerably, in particular because subtraction diagrams are introduced [61]. This changes the calculated value of  $k_{\text{SMS}}$  considerably, although the NMS coefficients change by less than  $\sim 10\%$ . The difference between the four-valence-electron and two-valence-electron (particle-hole) calculation is used to estimate the theoretical uncertainty.

TABLE I. The atomic transitions studied in tin. The upper and lower energy levels are provided from Ref. [41], which are compared to the calculated FSCC values. The calculated values agree with the experimental data within less than 2%.

Transition	$E_{\text{lower}}$ ( $\text{cm}^{-1}$ )	$E_{\text{upper}}$ ( $\text{cm}^{-1}$ )	$E_{\text{lower}}^{\text{FSCC}}$ ( $\text{cm}^{-1}$ )	$E_{\text{upper}}^{\text{FSCC}}$ ( $\text{cm}^{-1}$ )
$5s^2 5p^2 \ ^3P_1 \rightarrow 5s^2 5p6s^1 P_1$	1691.806	39257.053	1671	39124
$5s^2 5p^2 \ ^3P_1 \rightarrow 5s^2 5p6s^3 P_2$	1691.806	38628.876	1671	38471
$5s^2 5p^2 \ ^1S_0 \rightarrow 5s^2 5p7s^1 P_1$	17162.499	52706.832	17176	53331
$5s^2 5p^2 \ ^3P_2 \rightarrow 5s^2 5p6s^3 P_2$	3427.673	38628.876	3361	38471
$5s^2 5p^2 \ ^3P_0 \rightarrow 5s^2 5p6s^3 P_1$	0.000	34914.282	0	34767

## IV. RESULTS

### A. Atomic transitions and fine-structure levels

The transitions in Table I were studied using the laser-ionization schemes presented in Fig. 2. The calculated upper and lower level energies are compared to the experimental values in Table I. In the ground-state multiplet, the energy of the  $5p^2 \ ^3P_1$  and  $5p^2 \ ^3P_2$  levels is calculated with an accuracy of 1% and 2%, respectively, while for the excited states, an accuracy of less than 0.5% is achieved for all levels, except for the  $5p6s \ ^3P_2$  level where it is 1%. Using these transitions, the spectra of  $^{124-116}\text{Sn}$  shown in Fig. 3 were acquired with an acceleration potential of 20 kV. The  $^3P_0 \rightarrow ^3P_1$  transition

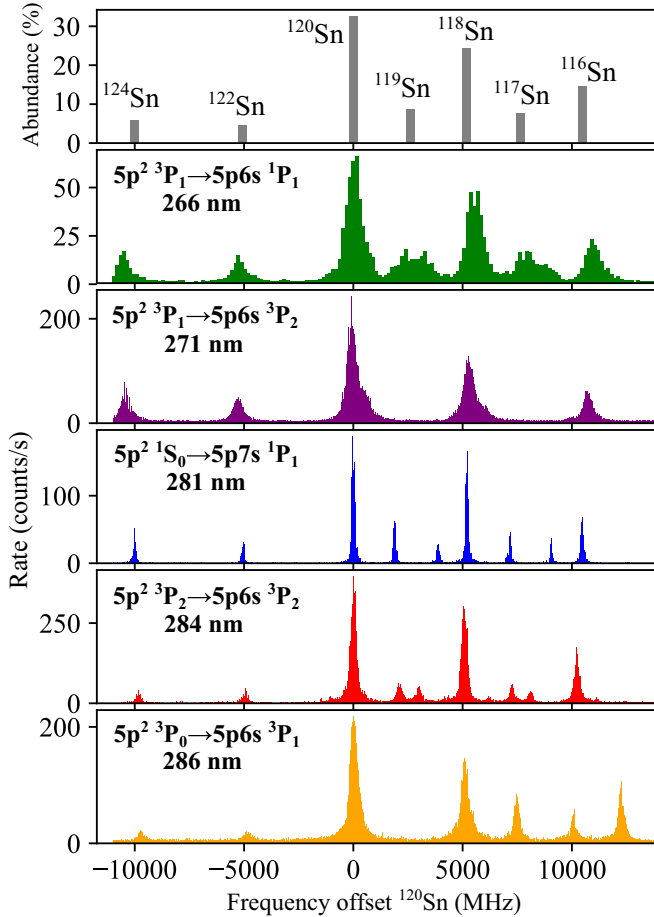


FIG. 3. Measured spectra of  $^{116-124}\text{Sn}$  using laser-ionization schemes presented in Fig. 2. The abundances and center-of-mass location of the different isotopes are indicated on the top.

was also obtained using a 30 kV acceleration potential. That is because overlapping resonances were observed at the lower beam energy.

The peak shapes could be approximated with Voigt profiles with 200 to 600 MHz total FWHM, dominated by the Lorentzian contribution. Indeed, the upper state lifetimes, of the order of a few nanoseconds [39], were significantly smaller than the laser pulse length, thus requiring temporal overlap of the laser pulses. This resulted in power-broadening effects, induced by interactions with the high-power second and third laser steps [66]. Additionally, the velocity distribution of the ion beam causes an asymmetry of the peak profile, which is discussed further in Sec. IV C. Tin isotopes with a natural abundance higher than 4%,  $^{116-124}\text{Sn}$  were observed with all ionization schemes. The isotopes  $^{112,114,115}\text{Sn}$  with abundances below 1% could be resolved using the ionization schemes for the  $^1S_0 \rightarrow ^1P_1$  and  $^3P_2 \rightarrow ^3P_2$  transitions. These measurements indicate an abundance of 0.30(15)% of the least abundant stable isotope  $^{115}\text{Sn}$  based on peak intensity ratios, in good agreement with the natural abundance in the literature [67]. For the three-step schemes, the dominant source of background was identified as nonresonant laser ionization due to the intermediate resonant step. This contribution accounted for roughly 80% of the observed background signal. This intermediate-step laser ionizes higher-lying atomic states populated during charge exchange, which were not field ionized before the interaction region. The remaining background was predominantly caused by collisional ionization after the interaction region, where a higher pressure of  $10^{-8}$  mbar was present.

### B. Isotope shifts and the hyperfine structure

The isotope shifts were determined from the difference in centroid frequencies  $\nu^A$  in the rest frame of the atoms, using  $\delta\nu^{A,A'} = \nu^A - \nu^{A'}$ , where  $A'$  is the reference isotope chosen as  $^{120}\text{Sn}$  due to its large relative abundance. For nonzero nuclear spin isotopes, the atomic fine-structure levels further break their degeneracy into a hyperfine structure, which can be calculated using the following expression:

$$\Delta E_{\text{hf}} = \frac{A_{\text{hf}}C}{2} + \frac{B_{\text{hf}}}{8} \frac{3C(C+1) - 4IJ(I+1)(J+1)}{IJ(2I-1)(2J-1)}, \quad (8)$$

with  $C = F(F+1) - J(J+1) - I(I+1)$ , and  $F$  takes integer steps between  $|J-I| < F < J+I$ , where  $I$  and  $J$  are the nuclear spin and electronic total angular momenta, respectively. The first dipole term is proportional to  $A_{\text{hf}} = gA_0$ , where  $A_0$  is the magnetic field contribution at the core

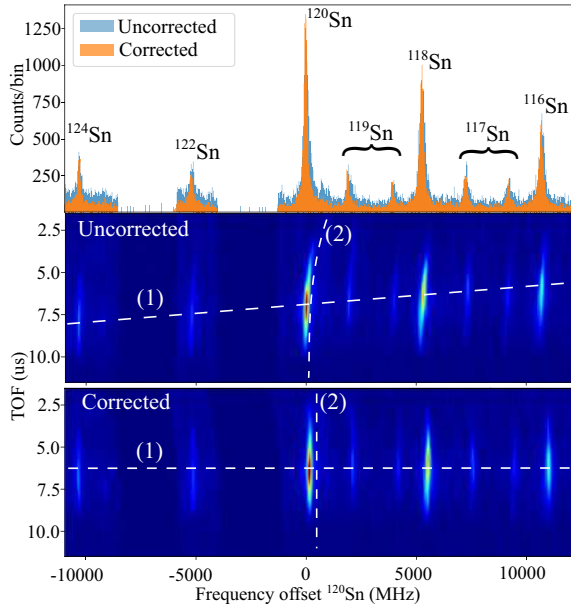


FIG. 4. Demonstration of TOF vs frequency correction procedure for the  $^1S_0 \rightarrow ^1P_1$  transition. The applied correction procedure involves two steps: (1) the resonances of all isotopes are shifted to have the same median TOF and (2) the bananalike shape for each resonance is corrected according to the curvature of the reference isotope  $^{120}\text{Sn}$ , reducing the linewidth and asymmetry of the final spectrum. The uncorrected and corrected histograms are projected at the top of the figure using 25 MHz bin size.

generated by the electrons, and  $g = \mu_I/I$  is the ratio of the nuclear magnetic dipole moment  $\mu_I$  to the nuclear spin  $I$ . The second term in Eq. (8) accounts for the electric quadrupole contribution and is proportional to  $B_{\text{hf}} = qQ_s$ , where  $q$  is the EFG generated by the electrons and  $Q_s$  is the spectroscopic electric quadrupole moment of the nucleus. This term is nonzero for  $J, I > 1/2$ . As the stable odd-mass isotopes,  $^{115}, ^{117}, ^{119}\text{Sn}$ , have a ground-state nuclear spin  $I = 1/2$ , no quadrupole interactions can be studied with stable tin isotopes, and therefore the second term does not play a role in the analysis of the data.

### C. Data-analysis procedure

Using the two-dimensional (2D) histogram of the TOF versus laser frequency, shown in Fig. 4, two corrections are applied. Initially, by gating on laser frequencies corresponding to the resonance signal for a specific tin isotope, TOF histograms for the different isotopes can be obtained. TOF histograms have a width of about 5(1)  $\mu\text{s}$ . The median of the TOF histogram for each isotope is observed to exhibit a mass dependence, linear in first order, with an average slope of 150(50) ns/u at a beam energy of 20 000(50) eV. These TOF histograms for each selected mass were shifted to match the median of the TOF for the reference isotope  $^{120}\text{Sn}$ ; see step (1) in Fig. 4. Shifting all masses to the same TOF allowed the use of a single TOF gate for all isotopes, conveniently reducing unwanted background without losing statistics. In a second step, as demonstrated in Ref. [34], the bananalike shape observed in the uncorrected TOF histogram in Fig. 4 for each of

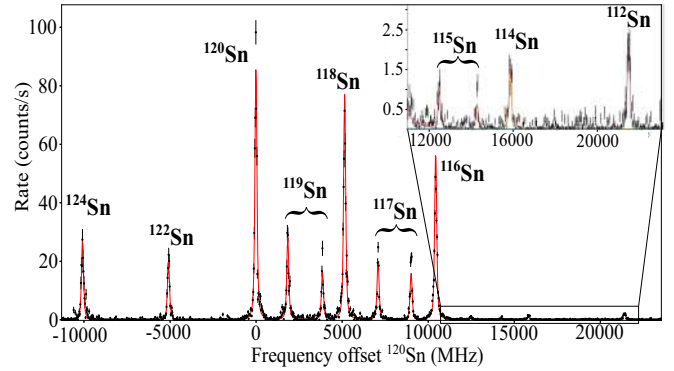


FIG. 5. A sample spectrum of the  $^1S_0 \rightarrow ^1P_1$  transition. All stable isotopes can clearly be identified, including  $^{115}\text{Sn}$  with a measured abundance of 0.30(15)%.

the isotope resonances is corrected. This shape is induced by an asymmetric ion velocity distribution, with a high velocity component from inhomogeneities in the extraction potential at the ion source and plasma-related effects from the ablation process [34]. Thus, ions with a different TOF experience a different Doppler shift, which effectively increases the linewidth in the laser scan and generates a tail extending towards higher frequencies. In order to correct for this energy spread, the data were subdivided in different TOF slices, 200–500 ns in width. The frequency spectrum obtained for each of these slices was then fitted with a Voigt profile using a  $\chi^2$ -minimization fitting routine to obtain the peak centroid. The centroids for each TOF slice show a clear correlation with the TOF, which is well approximated by the function  $f(t) = k/t + c$ . In this function,  $f(t)$  is a frequency offset with respect to the TOF  $t$ , while  $k$  and  $c$  are free fit parameters. The frequency shift with respect to TOF for  $^{120}\text{Sn}$  was used to correct the spectrum including all isotopes. The result is shown in Fig. 4, correction (2), leading to straight lines in the corrected TOF versus frequency plot. After the correction procedure, the total linewidth in the hyperfine spectrum is reduced and the background is suppressed as presented in the spectrum on top of Fig. 4. As an example, for the  $^1S_0 \rightarrow ^1P_1$  transition, the total FWHM decreased from 253(5) to 173(4) MHz. The significance of this correction depends on the experimental conditions of the ion source. This correction procedure could be applied to the spectra obtained with the  $^1S_0 \rightarrow ^1P_1$ ,  $^3P_2 \rightarrow ^3P_2$ , and  $^3P_0 \rightarrow ^3P_1$  transitions, where accurate TOF data were available.

The corrected spectra were then fitted with a Voigt profile using  $\chi^2$  minimization, enabling extraction of magnetic hyperfine constants and centroid frequencies using the SATLAS analysis package [68]. A fitted spectrum of the  $^1S_0 \rightarrow ^1P_1$  transition can be seen in Fig. 5. Each spectrum was fitted with various bin sizes in order to determine the dependence of the extracted parameters on the chosen bin size. The uncertainty associated with the TOF correction procedure is determined from the centroid scattering around the weighted mean of all fitted TOF slices. The combination of these contributions is listed in Table II as “Data processing unc.” since they are solely due to the data-handling procedure. Table II lists other uncertainties as well. The dominant source of uncertainty for the isotope shifts was associated with the ion beam energy, with an estimated stability of 0.001% of the set acceleration

TABLE II. Main sources of systematic errors identified from the extraction of isotopic shift and the hyperfine  $A_{\text{hf}}$  value for the  $^3P_2$  state of  $^{117}\text{Sn}$  using the  $^3P_2 \rightarrow ^3P_2$  transition.

	$A_{\text{hf}}^{117}$ (MHz)	$\delta v^{120,117}$ (MHz)
Value	-1546.0	-463.1
Data processing unc.	7.5	7.3
Ion beam energy	3.2	10.5
Wave-meter calib.	0.6	2.8
Total systematic unc.	8.2	13.1

voltage, and was furthermore only known with an accuracy of  $\pm 50$  V. The uncertainty due to laser frequency calibration, and possible nonlinearities from the wave-meter readout, are listed as the “wave-meter calib.” uncertainty.

The extracted  $A_{\text{hf}}$  constants for the different atomic states, seen in Table III, are compared with the literature values [22,23,69]. For  $^{115}\text{Sn}$ ,  $A_{\text{hf}}$  of the  $5p^2\ ^3P_2$  state was fixed to a high-precision measurement from Ref. [69] during fitting of the data, obtained with the  $^3P_2 \rightarrow ^3P_2$  transition, required as a constraint due to the low statistics. Similarly, for  $^{119}\text{Sn}$  and  $^{117}\text{Sn}$ ,  $A_{\text{hf}}$  of the  $5p^2\ ^3P_1$  state was fixed for the  $^3P_1 \rightarrow ^1P_1$  transition. Additionally, the ratio of  $A_{\text{hf}}$  for  $^{117,119}\text{Sn}$  was fixed to the same ratio as their nuclear magnetic moments from Ref. [25] for the  $5p6s\ ^1P_1$  state. The  $A_{\text{hf}}$  constants are in good agreement with the literature within  $1\sigma$  of the total uncertainty for all levels. Additionally, the isotope shifts using  $^{120}\text{Sn}$  as reference are presented in Table IV. The isotope shifts of the  $^3P_0 \rightarrow ^3P_1$  transition are compared with data from Ref. [22], indicating a close agreement with the literature.

## V. DISCUSSION

### A. Evaluating field- and mass-shift factors

The isotope shift is well approximated by the summed contribution from the field- and mass-shift terms accordingly,

$$\delta v^{A,A'} = F_\lambda \delta \langle r^2 \rangle^{A,A'} + k_{\text{MS}} \mu^{A,A'}. \quad (9)$$

Here,  $\delta \langle r^2 \rangle^{A,A'}$  is the difference in mean-squared nuclear charge radii and  $\mu^{A,A'} = \frac{m_A - m_{A'}}{m_A m_{A'}}$  is the reduced mass factor, where  $m$  is the atomic mass. The field-shift factor  $F_\lambda$  corresponds to the change of electronic charge density at the site of the nucleus, and thus determines the sensitivity to the change in the nuclear charge radius. The mass-shift factor  $k_{\text{MS}}$  is the sum of the normal ( $k_{\text{NMS}}$ ) and specific ( $k_{\text{SMS}}$ ) mass shifts. In order to extract  $F_\lambda$  and  $k_{\text{MS}}$  for each transition, a King-plot

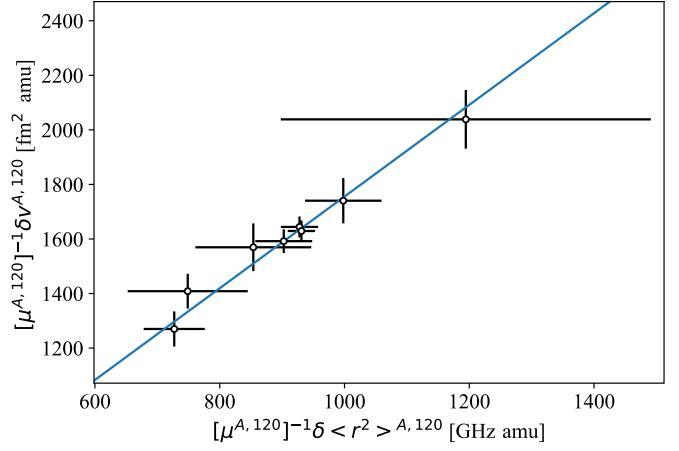


FIG. 6. King plot using Eq. (10) of the  $^1S_0 \rightarrow ^1P_1$  transition with  $^{120}\text{Sn}$  as a reference.

method as described in Ref. [70] was used, where the inverse of the reduced mass factor is multiplied on both sides of Eq. (9),

$$[\mu^{A,A'}]^{-1} \delta v^{A,A'} = F_\lambda [\mu^{A,A'}]^{-1} \delta \langle r^2 \rangle^{A,A'} + k_{\text{MS}}, \quad (10)$$

revealing a linear trend with slope  $F_\lambda$  and intercept  $k_{\text{MS}}$ . The isotope shifts in Table IV for each transition are compared with mean-squared nuclear charge radii determined from the combined analysis of muonic x-ray, electron-scattering, and optical data provided in Ref. [71] with a reduced mass factor calculated using masses from Ref. [72]. The King plot for each transition was fitted using orthogonal distance regression, which provides  $F_\lambda$  and  $k_{\text{MS}}$  from the slope and intercept. A sample King plot for the  $^1S_0 \rightarrow ^1P_1$  transition is shown in Fig. 6. Separate King plots were created using  $^{116,118,120}\text{Sn}$  as reference isotopes for each transition and the average  $F_\lambda$  and  $k_{\text{MS}}$  were selected for the final experimental values, with uncertainties determined from the standard deviation of the scatter summed in quadrature with the average sample error. Due to the lower statistics, the odd-mass isotopes were excluded from the King-plot analysis of the  $^3P_1 \rightarrow ^1P_1$  transition.

$F_\lambda$  and  $k_{\text{MS}}$  determined from experiment are compared to those from the atomic calculations, as described in Sec. III, and to the previous literature values for the  $^3P_0 \rightarrow ^3P_1$  transition in Table V. Most transitions have similar values of  $F_\lambda$ , thus all being similarly sensitive to a change in the nuclear charge radius. Only the  $^1S_0 \rightarrow ^1P_1$  transition has a

TABLE III. Hyperfine  $A_{\text{hf}}$  constants (in MHz) for  $^{115,117,119}\text{Sn}$ , compared with the literature (<sup>a</sup>Ref. [69], <sup>b</sup>Ref. [22], and <sup>c</sup>Ref. [23]). Statistical uncertainties are given in parentheses and experimental systematic uncertainties are given with square brackets.

Level	$A_{\text{Exp}}^{115}$	$A_{\text{Lit}}^{115}$	$A_{\text{Exp}}^{117}$	$A_{\text{Lit}}^{117}$	$A_{\text{Exp}}^{119}$	$A_{\text{Lit}}^{119}$
$5p^2\ ^3P_1$		507.445(4) <sup>a</sup>	695(83) [130]	552.608(4) <sup>a</sup>	452(82) [85]	578.296(4) <sup>a</sup>
$5p^2\ ^3P_2$		-1113.770 (4) <sup>a</sup>	-1211(9) [8]	-1212.956(3) <sup>a</sup>	-1269(6) [7]	-1269.419(3) <sup>a</sup>
$5p6s\ ^3P_1$		-4394.16(14) <sup>b</sup>	-4782(9) [22]	-4785.45(17) <sup>b</sup>	-5026(7) [25]	-5007.95(17) <sup>b</sup>
$5p6s\ ^3P_2$	-1438(9) [16]		-1546(9) [8]		-1621(6) [7]	
$5p6s\ ^1P_1$		-225.7 (9) <sup>c</sup>	-254(28) [23]	-247.6 (2) <sup>c</sup>	-266(29) [24]	-260.2 (2) <sup>c</sup>
$5p7s\ ^1P_1$	-1185(8) [13]		-1269(3) [12]		-1336(3) [11]	



TABLE IV. Measured isotope shifts (in MHz). Statistical uncertainties are indicated with parentheses and experimental systematic uncertainties are indicated with square brackets. For the  ${}^3P_0 \rightarrow {}^3P_1$  transition, a comparison is made to the literature [22].

Isotope	$\delta\nu_{1S_0 \rightarrow 1P_1}^{A,120}$	$\delta\nu_{3P_2 \rightarrow 3P_2}^{A,120}$	$\delta\nu_{3P_1 \rightarrow 3P_2}^{A,120}$	$\delta\nu_{3P_1 \rightarrow 1P_1}^{A,120}$	$\delta\nu_{3P_0 \rightarrow 3P_1}^{A,120}$	$\delta\nu_{3P_0 \rightarrow 3P_1}^{A,120}$ [22]
124	342(3) [17]	462(10) [15]	415(8) [29]	479(28) [15]	449(19) [20]	441.15(15)
122	192(3) [8]	228(11) [10]	214(9) [34]	238(29) [14]	270(15) [26]	235.35(15)
120	0	0	0	0	0	0
119	-142(2) [7]	-175(6) [8]	-166(17) [28]	-176(68)[93]	-211(7) [18]	-179.59(12)
118	-222(2) [12]	-267(4) [10]	-273(8) [33]	-263(17) [13]	-263(7) [18]	-270.24(15)
117	-372(3) [18]	-463(5) [13]	-467(41) [96]	-649(81) [23]	-494(9) [19]	-471.43(12)
116	-458(2) [12]	-580(6) [16]	-577(17) [26]	-622(15) [33]	-603(14) [39]	-576.04(15)
115	-637(5) [19]	-828(15) [19]				-804.92(12)
114	-722(5) [16]	-911(8) [23]				-900.68(15)
112	-971(5) [22]	-1253(6) [29]				-1218.29(15)

reduced  $F_\lambda$  by roughly 30% compared to the other transitions. Multiple independent studies have been performed using the  ${}^3P_0 \rightarrow {}^3P_1$  transition with varying estimates for the field-shift factor, i.e., 2390(270) [23], 3300(270) [24], 2180(170) [71], and 2740(570) MHz/fm<sup>2</sup> [20], and the mass-shift factor, i.e., -761(200) [24], 83(147) [71], and -455(479) GHz amu [20]. The weighted mean of these values for the  ${}^3P_0 \rightarrow {}^3P_1$  transition, with weights  $1/\sigma^2$  and errors scaled with the reduced  $\chi^2$ , is presented in Table V. Both the experimental value and the calculation are in close agreement with the literature for both  $F_\lambda$  and  $k_{MS}$  for this transition. However, the calculations indicate a better agreement with the lower bound of the literature  $F_\lambda$  and upper bound of the literature  $k_{MS}$ , which are closer to the values determined in Ref. [71]. The overall agreement between the calculated and experimental values for each transition is very good, demonstrating that modern relativistic approaches are capable of producing reliable field- and mass-shift factors for many-electron atoms such as tin.

Using the measured isotope shifts given in Table IV, combined with the calculated  $F_\lambda^{\text{FSCC}}$  and  $k_{MS}^{\text{CI+MBPT}}$  for each transition, independent sets of mean-squared nuclear charge radii can be deduced accordingly,

$$\delta\langle r^2 \rangle^{A,A'} = \frac{1}{F_\lambda^{\text{FSCC}}} (\delta\nu^{A,A'} - \mu^{A,A'} k_{MS}^{\text{CI+MBPT}}). \quad (11)$$

The rms charge radii  $R_{\text{rms}} = \sqrt{\delta\langle r^2 \rangle^{A,A'} + \langle r^2 \rangle^{A'}}$  of the stable tin isotopes are determined using  ${}^{120}\text{Sn}$  as a reference:  $\langle r^2 \rangle^{1/2} = 4.654(1)$  fm [71]. As an example, the resulting radii determined using isotope shifts from the  ${}^3P_2 \rightarrow {}^3P_2$  and  ${}^1S_0 \rightarrow {}^1P_1$  transitions are displayed in Fig. 7 and compared

with radii from a combined analysis provided in Ref. [71]. This shows the good agreement with literature with only a slight deviation, well within the theoretical uncertainties. The high precision of the data reveals the small odd-even staggering effect displayed in the inset of Fig. 7, which is in excellent agreement with the literature and can provide an interesting insight into the nuclear structure [2].

## B. Hyperfine magnetic fields

The hyperfine magnetic field contribution to  $A_{\text{hf}}$  can be decoupled from nuclear-structure effects by dividing with  $\mu_I/I$ :  $A_0 = A_{\text{hf}}I/\mu_I$ . The  $A_0$  value for each transition was extracted from the experimental  $A_{\text{hf}}$  of the three spin-1/2 isotopes, using magnetic dipole moments provided in Ref. [25]. The weighted means of  $A_0$  from the three isotopes is presented in Table VI for each studied atomic level. All values are in close agreement with those from the literature, as well as with the calculated values from FSCC theory, visualized in Fig. 8(a). Atomic states with a larger magnetic hyperfine field are more sensitive for the measurement of nuclear magnetic moments. The hyperfine magnetic field varies significantly among the the atomic configurations, with the  $5p6s {}^3P_1$  state exhibiting the greatest sensitivity.

## C. Electric-field gradients

The EFGs calculated using the relativistic FSCC method are presented in Table VII and can be seen in Fig. 8(b). Confidence in the accuracy of the calculated EFGs is provided by the good agreement of  $F_\lambda$  and  $A_{\text{hf}}$  with the experimental results. Additionally, the EFGs of the  $5p6s {}^1P_1$  and  $5p6s {}^3P_1$

TABLE V. Calculated and experimental field- and mass-shift factors. The weighted mean of the experimentally determined field-shift factors from Refs. [20,23,24,71] and mass-shift factors from Refs. [20,24,71] for the  ${}^3P_0 \rightarrow {}^3P_1$  transition are shown in bold.

Transition	Field shift (MHz/fm <sup>2</sup> )			Mass shift (GHz amu)				
	$F_\lambda^{\text{FSCC}}$	$F_\lambda^{\text{Exp}}$	$F_\lambda^{\text{Lit}}$	$k_{NMS}^{\text{CI+MBPT}}$	$k_{SMS}^{\text{CI+MBPT}}$	$k_{MS}^{\text{CI+MBPT}}$	$k_{MS}^{\text{Exp}}$	$k_{MS}^{\text{Lit}}$
${}^1S_0 \rightarrow {}^1P_1$	1552(233)	1584(209)		519	-409	110(300)	160(184)	
${}^3P_2 \rightarrow {}^3P_2$	2217(89)	2024(184)		604	-427	177(300)	205(160)	
${}^3P_1 \rightarrow {}^3P_2$	2200(88)	2323(395)		630	-436	193(300)	-116(328)	
${}^3P_1 \rightarrow {}^1P_1$	2104(84)	2932(1083)		645	-472	174(300)	-460(890)	
${}^3P_0 \rightarrow {}^3P_1$	2202(88)	2831(546)	<b>2452(240)</b>	598	-431	167(300)	-424(455)	<b>-160(312)</b>

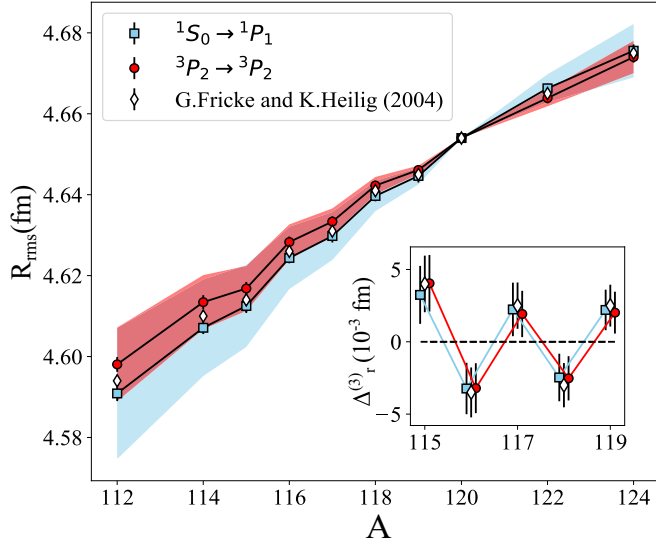


FIG. 7. The rms charge radii determined from the  ${}^3P_2 \rightarrow {}^3P_2$  and  ${}^1S_0 \rightarrow {}^1P_1$  transitions using Eq. (11) compared to the literature [71]. The total experimental uncertainty is indicated with error bars, and the theoretical uncertainty from  $k_{\text{MS}}^{\text{CI+MBPT}}$  and  $F_{\lambda}^{\text{FSCC}}$  is represented with color-coded bands. The inset displays the three-point odd-even staggering parameter  $\Delta_r^{(3)} = \frac{1}{2}(R_{A+1} - 2R_A + R_{A-1})$  highlighting the small odd-even staggering effect that becomes visible thanks to the high precision of the data.

states were calculated in Ref. [23] and, more recently, using a wide variety of advanced computational approaches in Refs. [25,73]. All of them are in good agreement with the values calculated in this work. An accurate understanding of EFGs is essential for the determination of the electric quadrupole moments. From this work, the  $5p6s\ {}^3P_2$  state is identified to have the highest sensitivity to  $Q_s$ .

#### D. Summary

Isotope shifts and hyperfine magnetic fields have been extracted using five atomic transitions in tin. State-of-the-art relativistic FSCC calculations provide the isotope-independent hyperfine magnetic field parameters of the atomic levels, showing excellent agreement with experiment. Additionally, these calculations provide EFGs, which are not accessible through atomic spectroscopy measurements of the stable tin isotopes and are essential for studying the electric quadrupole

TABLE VI.  $A_0$  values (in MHz) from this work compared with FSCC calculations and the literature values deduced from Refs. [22,23,69] in Table III. The  $A_0$  values are determined using magnetic moments from Ref. [25] as  $A_0 = A_{\text{hf}}I/\mu_I$ .

Level	$A_0^{\text{Lit}}$	$A_0^{\text{Exp}}$	$A_0^{\text{FSCC}}$
$5p^2\ {}^3P_1$	-276.77(2)	-278(29) [34]	-257(10)
$5p^2\ {}^3P_2$	607.50(4)	607(2) [3]	598(24)
$5p6s\ {}^3P_1$	2396.71(15)	2402(3) [11]	2352(94)
$5p6s\ {}^3P_2$		777(2) [5]	783(31)
$5p6s\ {}^1P_1$	124.3(2)	127(10) [16]	145(13)
$5p7s\ {}^1P_1$		638(1) [8]	571(103)

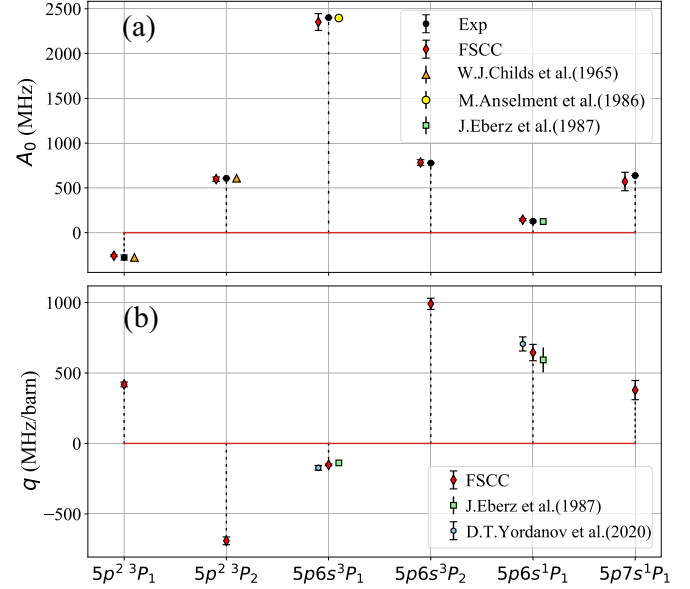


FIG. 8. (a) The  $A_0$  values are compared with theoretical predictions using the FSCC method and the literature data from Refs. [22,23,69]. (b) The calculated EFGs are displayed and compared with other calculated values from Refs. [23,25]. The dotted lines represent the sensitivity to  $\mu_I$  or  $Q_s$ , respectively. Only statistical errors are displayed for the experimental data from this work.

moment of the exotic tin nuclei using laser spectroscopy. According to these calculations, the  $5p6s\ {}^3P_2$  atomic level has the greatest sensitivity to the spectroscopic electric quadrupole moment, with an EFG roughly 50% greater compared to the  $5p6s\ {}^1P_1$  level used in previous work. The  $5p6s\ {}^3P_1$  level exhibits the greatest sensitivity to the nuclear magnetic moment, motivating its frequent use for probing the nuclear magnetic dipole moment. Furthermore, the large set of isotope shift measurements has been used for benchmarking the electronic  $F_{\lambda}$  and  $k_{\text{MS}}$  factors calculated using the combination of relativistic FSCC and CI+MBPT calculations. These calculations are in good agreement with experimentally obtained  $F_{\lambda}$  and  $k_{\text{MS}}$  factors of all studied transitions, allowing accurate determination of mean-square charge radii from isotope shift measurements.

In conclusion, this work demonstrates the reliability of modern atomic theory and provides a useful foundation for future measurements of the most short-lived exotic isotopes of tin from the evaluated sensitivity of several transitions to nuclear moments and mean-square nuclear charge radii.

TABLE VII. The EFGs (in MHz/b) calculated using FSCC compared with calculations from Refs. [23,25] with an estimated uncertainty of 15% for the values provided in Ref. [23].

Level	$q_{\text{Eberz}} [23]$	$q_{\text{MCDHF}} [25]$	$q_{\text{FSCC}}$
$5p^2\ {}^3P_1$			419(17)
$5p^2\ {}^3P_2$			-691(28)
$5p6s\ {}^3P_1$	-138(21)	-173(17)	-152(6)
$5p6s\ {}^3P_2$			990(40)
$5p6s\ {}^1P_1$	593(89)	706(50)	645(58)
$5p7s\ {}^1P_1$			378(68)

## ACKNOWLEDGMENTS

This work was supported by ERC Consolidator Grant No. 648381 (FNPMLS); STFC Grants No. ST/L005794/1, No. ST/L005786/1, and No. ST/P004423/1, and Ernest Rutherford Grant No. ST/L002868/1; KU Leuven Grant GOA 15/010 and grants from the FWO (Belgium); the European Unions Grant Agreement No. 654002 (ENSAR2); the U.S.

Department of Energy, Office of Science, Office of Nuclear Physics under Grant No. DE-SC0021176; National Key R&D Program of China (Contract No. 2018YFA0404403), and the National Natural Science Foundation of China (Grant No. 11875073). We would like to thank the Center for Information Technology of the University of Groningen for their support and for providing access to the Peregrine high-performance computing cluster.

- [1] P. Campbell, I. Moore, and M. Pearson, *Prog. Part. Nucl. Phys.* **86**, 127 (2016).
- [2] R. P. de Groote, J. Billowes, C. L. Binnersley, M. L. Bissell, T. E. Cocolios, T. Day Goodacre, G. J. Farooq-Smith, D. V. Fedorov, K. T. Flanagan, S. Franchoo, R. F. Garcia Ruiz, W. Gins, J. D. Holt, Á. Koszorus, K. M. Lynch, T. Miyagi, W. Nazarewicz, G. Neyens, P.-G. Reinhard, S. Rothe, H. H. Stroke, A. R. Vernon, K. D. A. Wendt, S. G. Wilkins, Z. Y. Xu, and X. F. Yang, *Nat. Phys.* **16**, 620 (2020).
- [3] R. F. Garcia Ruiz, M. L. Bissell, K. Blaum, A. Ekström, N. Frömmgen, G. Hagen, M. Hammen, K. Hebel, J. D. Holt, G. R. Jansen, M. Kowalska, K. Kreim, W. Nazarewicz, R. Neugart, G. Neyens, W. Nörtershäuser, T. Papenbrock, J. Papuga, A. Schwenk, J. Simonis, K. A. Wendt, and D. T. Yordanov, *Nat. Phys.* **12**, 594 (2016).
- [4] J. C. Berengut, D. Budker, C. Delaunay, V. V. Flambaum, C. Frugiuele, E. Fuchs, C. Grojean, R. Harnik, R. Ozeri, G. Perez, and Y. Soreq, *Phys. Rev. Lett.* **120**, 091801 (2018).
- [5] C. Delaunay, R. Ozeri, G. Perez, and Y. Soreq, *Phys. Rev. D* **96**, 093001 (2017).
- [6] C. Frugiuele, E. Fuchs, G. Perez, and M. Schlaffer, *Phys. Rev. D* **96**, 015011 (2017).
- [7] B. K. Sahoo, A. R. Vernon, R. F. Garcia Ruiz, C. L. Binnersley, J. Billowes, M. L. Bissell, T. E. Cocolios, G. J. Farooq-Smith, K. T. Flanagan, W. Gins, R. P. de Groote, Á. Koszorus, G. Neyens, K. M. Lynch, F. Parneffjord-Gustafsson, C. M. Ricketts, K. D. A. Wendt, S. G. Wilkins, and X. F. Yang, *New J. Phys.* **22**, 012001 (2020).
- [8] B. Ohayon, H. Rahangdale, A. J. Geddes, J. C. Berengut, and G. Ron, *Phys. Rev. A* **99**, 042503 (2019).
- [9] B. Cheal, T. E. Cocolios, and S. Fritzsche, *Phys. Rev. A* **86**, 042501 (2012).
- [10] H. Heylen, C. Babcock, R. Beerwerth, J. Billowes, M. L. Bissell, K. Blaum, J. Bonnard, P. Campbell, B. Cheal, T. Day Goodacre, D. Fedorov, S. Fritzsche, R. F. Garcia Ruiz, W. Geithner, C. Geppert, W. Gins, L. K. Grob, M. Kowalska, K. Kreim, S. M. Lenzi, I. D. Moore, B. Maass, S. Malbrunot-Ettenauer, B. Marsh, R. Neugart, G. Neyens, W. Nörtershäuser, T. Otsuka, J. Papuga, R. Rossel, S. Rothe, R. Sánchez, Y. Tsunoda, C. Wraith, L. Xie, X. F. Yang, and D. T. Yordanov, *Phys. Rev. C* **94**, 054321 (2016).
- [11] P. A. B. Haase, E. Eliav, M. Iliaš, and A. Borschevsky, *J. Phys. Chem. A* **124**, 3157 (2020).
- [12] S. A. Blundell, W. R. Johnson, and J. Sapirstein, *Phys. Rev. A* **43**, 3407 (1991).
- [13] S. G. Porsev, K. Beloy, and A. Derevianko, *Phys. Rev. D* **82**, 036008 (2010).
- [14] U. I. Safronova, *Phys. Rev. A* **81**, 052506 (2010).
- [15] X. F. Yang, C. Wraith, L. Xie, C. Babcock, J. Billowes, M. L. Bissell, K. Blaum, B. Cheal, K. T. Flanagan, R. F. Garcia Ruiz, W. Gins, C. Gorges, L. K. Grob, H. Heylen, S. Kaufmann, M. Kowalska, J. Kraemer, S. Malbrunot-Ettenauer, R. Neugart, G. Neyens, W. Nörtershäuser, J. Papuga, R. Sánchez, and D. T. Yordanov, *Phys. Rev. Lett.* **116**, 182502 (2016).
- [16] S. Kaufmann, J. Simonis, S. Bacca, J. Billowes, M. L. Bissell, K. Blaum, B. Cheal, R. F. Garcia Ruiz, W. Gins, C. Gorges, G. Hagen, H. Heylen, A. Kanellakopoulos, S. Malbrunot-Ettenauer, M. Miorelli, R. Neugart, G. Neyens, W. Nörtershäuser, R. Sánchez, S. Sailer, A. Schwenk, T. Ratajczyk, L. V. Rodríguez, L. Wehner, C. Wraith, L. Xie, Z. Y. Xu, X. F. Yang, and D. T. Yordanov, *Phys. Rev. Lett.* **124**, 132502 (2020).
- [17] R. Neugart, J. Billowes, M. L. Bissell, K. Blaum, B. Cheal, K. T. Flanagan, G. Neyens, W. Nörtershäuser, and D. T. Yordanov, *J. Phys. G* **44**, 064002 (2017).
- [18] T. Faestermann, M. Górka, and H. Grawe, *Prog. Part. Nucl. Phys.* **69**, 85 (2013).
- [19] T. D. Morris, J. Simonis, S. R. Stroberg, C. Stumpf, G. Hagen, J. D. Holt, G. R. Jansen, T. Papenbrock, R. Roth, and A. Schwenk, *Phys. Rev. Lett.* **120**, 152503 (2018).
- [20] C. Gorges, L. V. Rodríguez, D. L. Balabanski, M. L. Bissell, K. Blaum, B. Cheal, R. F. Garcia Ruiz, G. Georgiev, W. Gins, H. Heylen, A. Kanellakopoulos, S. Kaufmann, M. Kowalska, V. Lagaki, S. Lechner, B. Maaß, S. Malbrunot-Ettenauer, W. Nazarewicz, R. Neugart, G. Neyens, W. Nörtershäuser, P. G. Reinhard, S. Sailer, R. Sánchez, S. Schmidt, L. Wehner, C. Wraith, L. Xie, Z. Y. Xu, X. F. Yang, and D. T. Yordanov, *Phys. Rev. Lett.* **122**, 192502 (2019).
- [21] T. Togashi, Y. Tsunoda, T. Otsuka, N. Shimizu, and M. Honma, *Phys. Rev. Lett.* **121**, 062501 (2018).
- [22] M. Anselment, K. Bekk, A. Hanser, H. Hoeffgen, G. Meisel, S. Göring, H. Rebel, and G. Schatz, *Phys. Rev. C* **34**, 1052 (1986).
- [23] J. Eberz, U. Dinger, G. Huber, H. Lochmann, R. Menges, G. Ulm, R. Kirchner, O. Klepper, T. U. Köhl, and D. Marx, *Z. Phys. A* **326**, 121 (1987).
- [24] F. Le Blanc, L. Cabaret, E. Cottureau, J. E. Crawford, S. Essabaa, J. Genevey, R. Horn, G. Huber, J. Lassen, J. K. P. Lee, G. L. Scornet, J. Lettry, J. Obert, J. Oms, A. Ouchrif, J. Pinard, H. Ravn, B. Roussière, J. Sauvage, and D. Verney, *Phys. Rev. C* **72**, 034305 (2005).
- [25] D. T. Yordanov, L. V. Rodríguez, D. L. Balabanski, J. Bieroń, M. L. Bissell, K. Blaum, B. Cheal, J. Ekman, G. Gaigalas, R. F. Garcia Ruiz, G. Georgiev, W. Gins, M. R. Godefroid, C. Gorges, Z. Harman, H. Heylen, P. Jönsson, A. Kanellakopoulos, S. Kaufmann, C. H. Keitel, V. Lagaki, S. Lechner, B. Maaß, S.

- Malbrunot-Ettenauer, W. Nazarewicz, R. Neugart, G. Neyens, W. Nörtershäuser, N. S. Oreshkina, A. Papoulia, P. Pyykkö, P.-G. Reinhard, S. Sailer, R. Sánchez, S. Schiffmann, S. Schmidt, L. Wehner, C. Wraith, L. Xie, Z. Xu, and X. Yang, *Commun. Phys.* **3**, 107 (2020).
- [26] R. F. Garcia Ruiz, D. L. Balabanski, C. L. Binnersley, J. Billowes, M. Bissell, K. Blaum, T. E. Cocolios, R. P. de Groote, G. J. Farooq-Smith, K. T. Flanagan, S. Franchoo, G. Georgiev, Á. Koszorús, M. Kowalska, K. M. Lynch, S. Malbrunot-Ettenauer, B. A. Marsh, E. Minava Ramirez, P. Naubereit, G. Neyens, W. Nörtershäuser, S. Rothe, R. Sánchez, H. H. Stroke, D. Studer, A. R. Vernon, K. D. A. Wendt, S. G. Wilkins, Z. Xu, X. F. Yang, and D. T. Jordanov, Laser spectroscopy of neutron-deficient Sn isotopes, Tech. Rep. No. CERN-INTC-2016-006. INTC-P-456 (CERN, Geneva, 2016), Proposal to the ISOLDE and Neutron Time-of-Flight Committee.
- [27] R. Ferrer, B. Bastin, D. Boilley, P. Creemers, P. Delahaye, E. Liénard, X. Fléchar, S. Franchoo, L. Ghys, M. Huysse, Y. Kudryavtsev, N. Lece, H. Lu, F. Lutton, E. Mogilevskiy, D. Pauwels, J. Piot, D. Radulov, L. Rens, H. Savajols, J. C. Thomas, E. Traykov, C. Van Beveren, P. Van Den Bergh, and P. Van Duppen, *Nucl. Instrum. Methods B* **317**, 570 (2013).
- [28] P. Papadakis, I. Moore, I. Pohjalainen, J. Sarén, and J. Uusitalo, *Hyperfine Interact.* **237**, 1 (2016).
- [29] O. Kavatsyuk, C. Mazzocchi, Z. Janas, A. Banu, L. Batist, F. Becker, A. Blazhev, W. Brüchle, J. Döring, T. Faestermann, M. Górska, H. Grawe, A. Jungclaus, M. Karny, M. Kavatsyuk, O. Klepper, R. Kirchner, M. La Commara, K. Miernik, I. Mukha, C. Plettner, A. Płochocki, E. Roeckl, M. Romoli, K. Rykaczewski, M. Schädel, K. Schmidt, R. Schwengner, and J. Żylicz, *Eur. Phys. J. A* **31**, 319 (2007).
- [30] D. Studer, J. Ulrich, S. Braccini, T. S. Carzaniga, R. Dressler, K. Eberhardt, R. Heinke, U. Köster, S. Raeder, and K. Wendt, *Eur. Phys. J. A* **56**, 69 (2020).
- [31] A. Zadornaya, P. Creemers, K. Dockx, R. Ferrer, L. P. Gaffney, W. Gins, C. Granados, M. Huysse, Yu. Kudryavtsev, M. Laatiaoui *et al.*, *Phys. Rev. X* **8**, 041008 (2018).
- [32] K. T. Flanagan, K. M. Lynch, J. Billowes, M. L. Bissell, I. Budinčević, T. E. Cocolios, R. P. de Groote, S. De Schepper, V. N. Fedosseev, S. Franchoo, R. F. Garcia Ruiz, H. Heylen, B. A. Marsh, G. Neyens, T. J. Procter, R. E. Rossel, S. Rothe, I. Strashnov, H. H. Stroke, and K. D. A. Wendt, *Phys. Rev. Lett.* **111**, 212501 (2013).
- [33] T. E. Cocolios, R. P. de Groote, J. Billowes, M. L. Bissell, I. Budinčević, T. Day Goodacre, G. J. Farooq-Smith, V. N. Fedosseev, K. T. Flanagan, S. Franchoo, R. F. Garcia Ruiz, W. Gins, H. Heylen, T. Kron, R. Li, K. M. Lynch, B. A. Marsh, G. Neyens, R. E. Rossel, S. Rothe, A. J. Smith, H. H. Stroke, K. D. Wendt, S. G. Wilkins, and X. Yang, *Nucl. Instrum. Methods B* **376**, 284 (2016).
- [34] R. F. Garcia Ruiz, A. R. Vernon, C. L. Binnersley, B. K. Sahoo, M. Bissell, J. Billowes, T. E. Cocolios, W. Gins, R. P. de Groote, K. T. Flanagan, Á. Koszorús, K. M. Lynch, G. Neyens, C. M. Ricketts, K. D. A. Wendt, S. G. Wilkins, and X. F. Yang, *Phys. Rev. X* **8**, 041005 (2018).
- [35] A. R. Vernon, J. Billowes, C. L. Binnersley, M. L. Bissell, T. E. Cocolios, G. J. Farooq-Smith, K. T. Flanagan, R. F. Garcia Ruiz, W. Gins, R. P. de Groote, Á. Koszorús, K. M. Lynch, G. Neyens, C. M. Ricketts, K. D. A. Wendt, S. G. Wilkins, and X. F. Yang, *Spectrochim. Acta, Part B* **153**, 61 (2019).
- [36] R. P. de Groote, I. Budinčević, J. Billowes, M. L. Bissell, T. E. Cocolios, G. J. Farooq-Smith, V. N. Fedosseev, K. T. Flanagan, S. Franchoo, R. F. Garcia Ruiz, H. Heylen, R. Li, K. M. Lynch, B. A. Marsh, G. Neyens, R. E. Rossel, S. Rothe, H. H. Stroke, K. D. A. Wendt, S. G. Wilkins, and X. Yang, *Phys. Rev. Lett.* **115**, 132501 (2015).
- [37] T. Kessler, H. Tomita, C. Mattolat, S. Raeder, and K. Wendt, *Laser Phys.* **18**, 842 (2008).
- [38] Á. Koszorús, X. F. Yang, J. Billowes, C. L. Binnersley, M. L. Bissell, T. E. Cocolios, G. J. Farooq-Smith, R. P. de Groote, K. T. Flanagan, S. Franchoo, R. F. Garcia Ruiz, S. Geldhof, W. Gins, A. Kanellakopoulos, K. M. Lynch, G. Neyens, H. H. Stroke, A. R. Vernon, K. D. A. Wendt, and S. G. Wilkins, *Phys. Rev. C* **100**, 034304 (2019).
- [39] W. Zhang, Y. Feng, J. Xu, P. Palmeri, P. Quinet, É. Biémont, and Z. Dai, *J. Phys. B* **43**, 205005 (2010).
- [40] A. R. Vernon, R. P. de Groote, J. Billowes, C. L. Binnersley, T. E. Cocolios, G. J. Farooq-Smith, K. T. Flanagan, R. F. Garcia Ruiz, W. Gins, Á. Koszorús, G. Neyens, C. M. Ricketts, A. J. Smith, S. G. Wilkins, and X. F. Yang, *Nucl. Instrum. Methods B* **463**, 384 (2020).
- [41] A. Kramida, Yu. Ralchenko, J. Reader, and NIST ASD Team, NIST Atomic Spectra Database (ver. 5.7.1), <https://physics.nist.gov/asd> (National Institute of Standards and Technology, Gaithersburg, MD, 2019).
- [42] U. Kaldor and E. Eliav, *Adv. Quantum Chem.* **31**, 313 (1998).
- [43] L. Visscher, E. Eliav, and U. Kaldor, *J. Chem. Phys.* **115**, 9720 (2001).
- [44] L. Visscher and K. G. Dyall, *At. Data Nucl. Data Tables* **67**, 207 (1997).
- [45] A. Landau, E. Eliav, and U. Kaldor, *Adv. Quantum Chem.* **39**, 171 (2001).
- [46] J. A. Pople, J. W. McIver, and N. S. Ostlund, *J. Chem. Phys.* **49**, 2960 (1968).
- [47] H. Yakobi, E. Eliav, L. Visscher, and U. Kaldor, *J. Chem. Phys.* **126**, 054301 (2007).
- [48] L. Visscher, T. Enevoldsen, T. Saue, and J. Oddershede, *J. Chem. Phys.* **109**, 9677 (1998).
- [49] T. Saue, R. Bast, A. S. P. Gomes, H. J. A. Jensen, L. Visscher, I. A. Aucar, R. Di Remigio, K. G. Dyall, E. Eliav, E. Fasshauer *et al.*, *J. Chem. Phys.* **152**, 204104 (2020).
- [50] R. Bast, T. Saue, L. Visscher, and H. J. A. Jensen, with contributions from V. Bakken, K. G. Dyall, S. Dubillard, U. Ekstroem, E. Eliav, T. Enevoldsen, E. Fasshauer, T. Fleig, O. Fossgaard, A. S. P. Gomes, T. Helgaker, J. Henriksson, M. Ilias, Ch. R. Jacob, S. Knecht, S. Komorovsky, O. Kullie, J. K. Laerdahl, C. V. Larsen, Y. S. Lee, H. S. Nataraj, M. K. Nayak, P. Norman, G. Olejniczak, J. Olsen, Y. C. Park, J. K. Pedersen, M. Pernpointner, R. Di Remigio, K. Ruud, P. Salek, B. Schimmelpfennig, J. Sikkema, A. J. Thorvaldsen, J. Thyssen, J. van Stralen, S. Villaume, O. Visser, T. Winther, and S. Yamamoto, computer code DIRAC, a relativistic *ab initio* electronic structure program, release DIRAC15 (2015) (see <http://www.diracprogram.org>).
- [51] L. Visscher, H. J. A. Jensen, R. Bast, and T. Saue, with contributions from V. Bakken, K. G. Dyall, S. Dubillard, U. Ekström, E. Eliav, T. Enevoldsen, E. Fasshauer, T. Fleig, O. Fossgaard, A. S. P. Gomes, E. D. Hedegård, T. Helgaker, J. Henriksson, M. Iliáš, Ch. R. Jacob, S. Knecht, S. Komorovský, O. Kullie, J. K. Laerdahl, C. V. Larsen, Y. S. Lee, H. S. Nataraj, M. K.



- Nayak, P. Norman, G. Olejniczak, J. Olsen, J. M. H. Olsen, Y. C. Park, J. K. Pedersen, M. Pernpointner, R. di Remigio, K. Ruud, P. Sałek, B. Schimmelpfennig, A. Shee, J. Sikkema, A. J. Thorvaldsen, J. Thyssen, J. van Stralen, S. Villaume, O. Visser, T. Winther, and S. Yamamoto, DIRAC, a relativistic *ab initio* electronic structure program, release DIRAC17 (2017) (see <http://www.diracprogram.org>).
- [52] M. Iliaš and T. Saue, *J. Chem. Phys.* **126**, 064102 (2007).
- [53] R. Bast, A. J. Thorvaldsen, M. Ringholm, and K. Ruud, *Chem. Phys.* **356**, 177 (2009).
- [54] S. Knecht, H. J. A. Jensen, and T. Fleig, *J. Chem. Phys.* **132**, 014108 (2010).
- [55] G. Breit, *Phys. Rev.* **34**, 375 (1929).
- [56] K. G. Dyall, *Theor. Chem. Acc.* **115**, 441 (2006).
- [57] V. A. Dzuba, V. V. Flambaum, and M. G. Kozlov, *Phys. Rev. A* **54**, 3948 (1996).
- [58] E. V. Kahl and J. C. Berengut, *Comput. Phys. Commun.* **238**, 232 (2019).
- [59] W. R. Johnson, S. A. Blundell, and J. Sapirstein, *Phys. Rev. A* **37**, 307 (1988).
- [60] J. C. Berengut, V. V. Flambaum, and M. G. Kozlov, *Phys. Rev. A* **73**, 012504 (2006).
- [61] J. C. Berengut, *Phys. Rev. A* **94**, 012502 (2016).
- [62] J. C. Berengut, V. V. Flambaum, and E. M. Kava, *Phys. Rev. A* **84**, 042510 (2011).
- [63] A. N. Artemyev, V. M. Shabaev, and V. A. Yerokhin, *Phys. Rev. A* **52**, 1884 (1995).
- [64] V. M. Shabaev, *Phys. Rev. A* **57**, 59 (1998).
- [65] C. W. P. Palmer, *J. Phys. B* **20**, 5987 (1987).
- [66] R. P. De Groote, M. Verlinde, V. Sonnenschein, K. T. Flanagan, I. Moore, and G. Neyens, *Phys. Rev. A* **95**, 032502 (2017).
- [67] C. Devillers, T. Lecomte, and R. Hagemann, *Int. J. Mass Spectrom. Ion Phys.* **50**, 205 (1983).
- [68] W. Gins, R. P. de Groote, M. L. Bissell, C. Granados Buitrago, R. Ferrer, K. M. Lynch, G. Neyens, and S. Sels, *Comput. Phys. Commun.* **222**, 286 (2018).
- [69] W. J. Childs and L. S. Goodman, *Phys. Rev.* **137**, A35 (1965).
- [70] G. Fricke, C. Bernhardt, K. Heilig, L. Schaller, L. Schellenberg, E. Spera, and C. Dejager, *At. Data Nucl. Data Tables* **60**, 177 (1995).
- [71] G. Fricke and K. Heilig, *Nuclear Charge Radii, 50-Sn Tin: Datasheet from Landolt-Börnstein - Group I Elementary Particles, Nuclei and Atoms*, Vol. 20, in Springer Materials (Springer-Verlag, Berlin, 2004).
- [72] M. Wang, G. Audi, F. Kondev, W. Huang, S. Naimi, and X. Xu, *Chin. Phys. C* **41**, 030003 (2017).
- [73] A. Papoulia, S. Schiffmann, J. Bieroń, G. Gaigalas, M. Godefroid, Z. Harman, P. Jönsson, N. S. Oreshkina, P. Pyykkö, and I. I. Tupitsyn, [arXiv:2007.11419](https://arxiv.org/abs/2007.11419).